

Toward Appearance-based Autonomous Landing Site Identification for Multirotor Drones in Unstructured Environments

Joshua Springer^[0000-0003-0137-1770],
Gylfi Þór Guðmundsson^[0000-0003-0846-6617], and
Marcel Kyas^[0000-0003-1018-3413]

Reykjavik University, Iceland
{joshua19, gylfig, marcel}@ru.is

Abstract. A remaining challenge in multirotor drone flight is the autonomous identification of viable landing sites in unstructured environments. One approach to solve this problem is to create lightweight, appearance-based terrain classifiers that can segment a drone’s RGB images into safe and unsafe regions. However, such classifiers require data sets of images and masks that can be prohibitively expensive to create. We propose a pipeline to automatically generate synthetic data sets to train these classifiers, leveraging modern drones’ ability to survey terrain automatically and the ability to automatically calculate landing safety masks from terrain models derived from such surveys. We then train a U-Net on the synthetic data set, test it on real-world data for validation, and demonstrate it on our drone platform in real-time.

Keywords: Autonomous drone · terrain classifier · landing site · synthetic dataset · image segmentation · real-world validation.

1 Introduction

Autonomous multirotor drones are widely used in many fields, primarily as remote sensor platforms. While they excel at automated data collection, surveys, and other in-flight tasks, autonomous landing remains a challenge in locations other than the initial takeoff site or specially marked locations. Furthermore, many drones are blind to obstacles and other hazardous terrain conditions, as they primarily rely on GPS positioning at takeoff and landing. It is possible to increase landing accuracy and offer some obstacle avoidance by marking a safe landing site with a visual pattern, which the drone can locate via its (typically gimbal-mounted) RGB camera. However, this requires that the landing site should be known beforehand and that additional infrastructure – possibly even requiring power – should be in place. To make landing in an unstructured, previously unknown environment viable, the drone must first analyze its environment in flight using more complex sensors, e.g., LiDAR or stereo depth cameras. Such advanced sensors are effective but also computationally expensive and thus power-hungry, reducing task-oriented mission time. Alternatively,

the heavy computation can be offloaded to a ground station, but this requires added infrastructure and introduces problems with transmission overhead, connectivity, and latency.

We approach autonomous landing site identification as an image segmentation problem, with the goal of creating an appearance-based classifier that distinguishes safe and unsafe landing sites in images from our drone’s gimbal-mounted RGB camera. Image segmentation often requires a labeled data set, which is potentially prohibitively expensive to create manually. We can exploit drones’ strength in surveying terrain to easily build terrain models from which we can automatically generate a synthetic, labeled data set to circumvent this challenge. We prioritize keeping the computational overhead as low as possible as we run our solution onboard a drone in real time. We target the typical, gimbal-mounted RGB camera as our primary sensor instead of LiDAR, as the RGB camera is the most common drone peripheral sensor and will make the solution more generalizable and lightweight. Our contributions are as follows: (1) we present a pipeline to create synthetic image segmentation data sets for determining landing safety from terrain surveys (see Sections 3.3 and 3.4). (2) We present a method for creating small, but effective, real-world validation sets of videos taken of known-safe and known-unsafe landing sites in the real world to determine whether our method can bridge the gap from simulation to reality (see Section 3.2). Finally, (3) we showcase a U-Net trained on one such data set that is able to correctly classify 15 of 18 validation cases, which run in real-time onboard our drone platform.

We evaluate our work using the drone platform described in [23], which has previously been demonstrated successfully in the context of autonomous landing with an RGB camera and visual markers [22]. We have added a Google Coral TPU accelerator to run our tiny terrain classifier (under 1 MB in size). While the small classifiers are best suited to specific environment types, they are small enough that we can store multiple classifiers on an embedded computer that can use the most relevant one. On the other hand, the method for creating the classifiers is generalizable to any environment where there is some relationship between visual appearance and landing safety. The final stage of this process is the actual autonomous landing of the drone, which is out of the scope of this paper. Our approach of identifying a viable landing site in RGB video as an image segmentation problem, where we mark each pixel as safe or unsafe, will allow our system to choose a safe pixel position representing a target landing location. With minor future adaptations, our system will then be able to control the drone and carry out landings using the method described in [22], which lands the drone at a particular site specified by a pixel position.

2 Related Work

Landing site detection is similar to the notion of *traversability*, which has been explored extensively on ground vehicles. [4] presents a survey of ground vehicle traversability methods, dividing them generally into appearance-based,

geometric-based, and mixed methods. Appearance-based methods analyze terrain using visual sensors, whereas geometric-based methods require sensors such as LiDAR or RGBD that can extract a 3D representation of the environment. Some methods show success in traversability analysis, where training data is collected and labeled directly with 3D sensors, and terrain classification is performed with visual sensors only [3,26]. Some others classify 3D data from LiDAR and RGBD cameras directly [25]. There is also a tendency to classify each pixel into one of three groups, e.g., traversable, not traversable, and unknown. These methods typically do not analyze reconstructed terrain models, but instead, analyze the terrain directly via some sensor and apply that analysis to label RGB images. Many traversability methods are developed and tested in simulation, but the gap from simulation to reality is often not overcome. While appearance-based methods can lack accuracy, they only require simple RGB camera sensors that are abundant, cheaper, and have a lower processing overhead than the hardware needed for geometric-based methods [4]. Many of the methods presented require specialized data sets with multiple data sources, i.e., RGB and at least one LiDAR or RGBD, to determine a label for the terrain.

Most work in autonomous landing site identification in unstructured environments is geometric-based, requiring real-time LiDAR or RGBD analysis, full-size GPUs, etc. [12,5]. However, some methods visually locate their starting location using its visual appearance only [19]. More general appearance-based methods in this context are less widespread, as they often depend on expensive, manually-labeled data sets. In this context, some methods exist to sparsely label video frames manually, and then propagate the labels from frame to frame [16]; others use previously trained neural networks to add new labels to drone videos [18]. These methods have not yet been applied to autonomous landing but have potential in identifying viable landing sites. Many methods are tested only in simulation or laboratory settings on real drone video but are not embedded onto the drone [24,18]. SafeUAV serves as an initial proof of concept for our proposed method [15]. It uses existing synthetic data sets from Google, making it possible to quickly extract training data from many locations but making the data less dynamic when the environment has recently changed. Their setup requires a camera at a fixed angle of 45° below the horizontal, and their classifiers predict the scene’s 3D depth and landing safety. Crucially, they consider the problem of embedding their classifiers on a drone in the real world and therefore test them on embeddable hardware (an NVIDIA Jetson TX2) and actual drone footage, although they do not deploy their solution on a drone.

We take inspiration from many of these papers and seek to create a full-pipeline approach that allows for flexibility in data requirements, minimizes manual labeling as much as possible, and ultimately produces a viable embedded terrain classifier that can run in real-time onboard a drone. To satisfy the real-time aspect, we prefer to use an appearance-based approach such that the classifier can perform inference on RGB images, which are lightweight to analyze when compared to, e.g., LiDAR data. This also makes the method easier to generalize to drone platforms without LiDAR or RGBD cameras. For flexibility



Fig. 1: One of three data collection sites. We manually and randomly picked 18 validation sites, and we number them as follows, marking safe with an S and unsafe with a U: (1U) – an archery target on a soccer field, (2U) – a bush, (3S) – a flat, dirt area, (4U) – a large, cracked rock mound, (5U) – high vegetation area, (6S) – flat, mossy area in a lava field, (7S) – flat, grassy area, (8S) – flat, mossy area in a lava field, (9U) – crack in a lava field, (10S) – dirt patch in a lava field, (11S) – road, (12U) – person, (13U) – very rough lava field, (14S) – model aircraft runway, (15U) – sloped, gravel edge of a soccer field, (16S) – green spot in a soccer field, (17S) – middle of a soccer field, (18U) – soccer goal. Map source: Loftmyndir ehf. [14]

in data requirements and ease in manual labeling, we generate intermediate 3D models from which we produce a synthetic data set of RGB images and masks. This gives the advantage that we can use many different data sources to generate the intermediate models, e.g., photogrammetry, LiDAR, RGBD, etc. This also means that we do not necessarily have to collect our data but can use openly available, standard-format, unlabeled data sets from terrain surveys. We also allow for the ability to quickly add manual labels to the intermediate models one time; such labels then propagate to all of the images generated. Importantly, we can vary the angle of our camera, which inherently makes the classifier more flexible than that in [15]. Finally, while we do not prescribe a particular, optimal classifier architecture, we create a successful U-Net that is relatively tiny (on the order of 1 MB instead of more than 1 GB) and can be deployed on power-efficient hardware compared to all methods described earlier. We also showcase how our classifier can be embedded onboard a drone.

3 Methods

We describe the process of collecting and transforming terrain data for our image segmentation purposes. We have automated this process except for logistical tasks such as transporting the drone to the survey location and optional, manual label refinement.

3.1 Data Acquisition – Terrain Surveys

The first step in generating data for the image segmentation problem is to collect terrain data from an environment similar to where a drone will need to land autonomously. For this purpose, we test both photogrammetry and LiDAR surveys, which have been automated in the case of many drones so that an operator needs only to select an area for surveying and then can deploy the drone to do the survey automatically. Photogrammetry is the process of combining images to create composite images or 3D models. We use ortho and oblique images in photogrammetry because this results in better 3D reconstructions of surfaces of all orientations. For example, when using primarily orthogonal images for terrain reconstruction, vertical surfaces can be severely distorted, as mentioned in [15]. LiDAR surveys provide similar terrain reconstruction capabilities as photogrammetry, but often with higher quality, higher data collection speed, and a higher price point – although this is not a hard rule. LiDAR produces point cloud data, which can be colorized by registering the points with RGB images collected simultaneously.

3.2 Data Acquisition – Validation Dataset

To generate a validation data set without frame-by-frame, manual labeling, we collect 10-second videos of particular validation sites in the field. In each video, the drone’s camera holds the validation site in the center of the frame, such that it collects many different frames from many different angles as the drone moves. The camera’s tilt is between 45° below the horizon and vertically down. We set the validation site to be either an obstacle or a clearing and record the classifier’s predictions of the center pixels of the video for all the frames, adjusting the central region’s size according to the validation site’s size. We tag each video as a whole according to whether it shows a safe landing site or not, and we compare our manual classification to the classifier’s predictions over the frames of the video. The prediction describes the classification of the majority of pixels in the central region of the video, and we aggregate it over time to determine a simple, binary prediction for the entire video. Some of the sites are hand-selected over a range of anticipated difficulties, considering the appearance-based classifier’s lack of geometric understanding of the scene it is classifying. For example, we expect the classifier to easily determine that an open field is safe and that a large crack in the ground is unsafe. On the other hand, we expect that it should be hard to classify slanted dirt areas as unsafe, since they appear visually similar to the safe, level dirt areas.

3.3 3D Terrain Model Reconstruction

The second step in generating our dataset, after conducting a survey or downloading an openly available survey, is to generate an RGB mesh that is a colorized, 3D depiction of the terrain. We create this mesh from photogrammetry

data using WebODM [27], or from LiDAR data by performing a Poisson reconstruction [13] in Cloudcompare [1].

The third step is to create a “label mesh” with the same topography as the RGB mesh that is marked according to which regions are safe and unsafe according to our geometric specifications. We sample the RGB mesh to create a point cloud with uniform density to calculate geometric features. This is necessary to remove “fuzziness” in point clouds derived from photogrammetry, and to remove scanning overlap in point clouds collected via LiDAR, since such variations can influence geometric features. We then calculate the normal vectors and geometric features of *verticality* – how slanted a region is – and *surface variation* – how rough a region is [10]. We compute a binary safety metric over the mesh, marking as unsafe all areas with verticality > 0.01 , surface variation > 0.002 (experimentally determined). We further eliminate unsafe areas that have been classified as safe geometrically, because of their low verticality and surface variation, e.g., lakes and rivers, by simply selecting them in CloudCompare and adding a manual classification to all the points representing the problematic surface. This process is quick, requiring only about 2 minutes to manually label the river of several hundred meters in Figure 2. We then apply Gaussian smoothing to the safety metric as the new grayscale texture for the label mesh. Finally, we slice the meshes into smaller chunks that are manageable on our hardware.

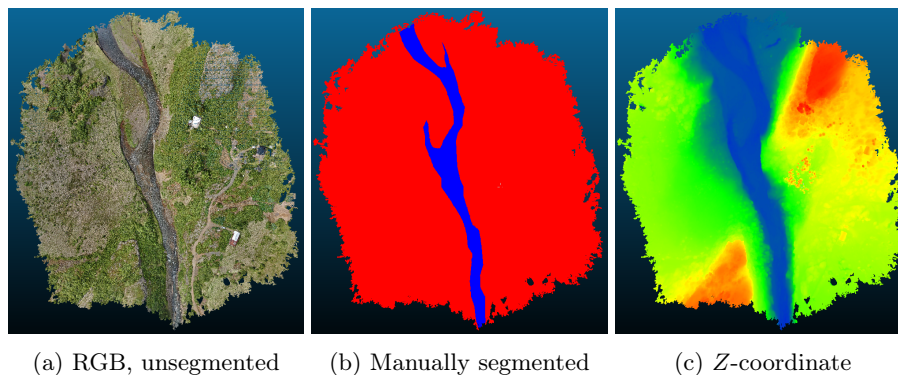


Fig. 2: Example of manual segmentation of a river in the summer house dataset by isolating the river and adding a manual classification to it in CloudCompare. It is not feasible to isolate the river by simply filtering on the altitude above sea level (ASL) since the terrain has a significant slope.

3.4 Synthetic Segmentation Dataset Generation

The fourth and last step in generating our data set is to create synthetic aerial images representing a drone’s view of the terrain and corresponding masks that

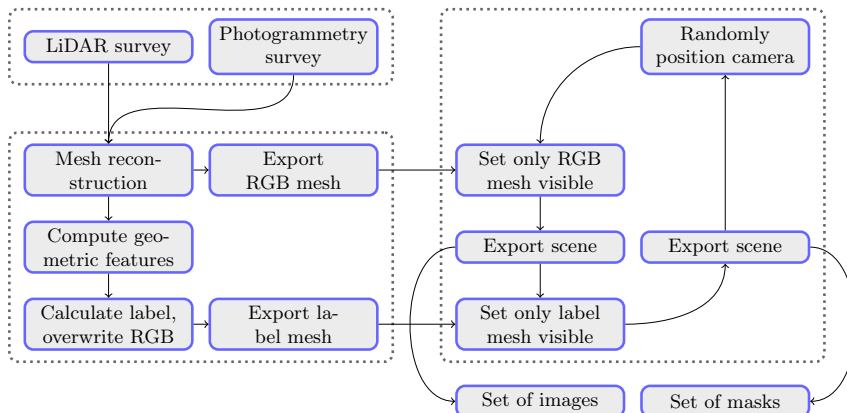


Fig. 3: Pipeline for creating labeled image datasets from terrain surveys.

specify which pixels in those images represent safe landing sites. Using NVIDIA Isaac Sim [7], we create a scene with the RGB and label meshes at the same position and orientation, with only one visible at a time. We position a virtual camera randomly in the scene, and aim it at a random location on the meshes, ensuring that the camera is between a minimum and maximum height above the terrain and between a minimum and maximum angular deflection from vertical down. We set the RGB mesh as visible and take a picture, effectively creating a typical aerial picture of a given terrain area. Then, we set the label mesh as visible and take another picture, creating a safety mask for the RGB image. We repeat this process for each slice to generate the labeled data set as many times as necessary. Figure 3 visualizes this process and Figure 4 shows examples from a dataset, where the terrain is shown on top, and masks are shown on the bottom. White and black areas indicate safe and unsafe areas for landing, respectively.

The following is a non-exhaustive list of changeable parameters which we have set experimentally and which may require special attention depending on the specific scenario: data collection altitude, image/pointcloud overlap, method and radius for calculating point cloud normal vectors, Poisson reconstruction parameters, radii for calculating verticality and planarity (as well as the corresponding thresholds), slice size, maximum height and deflection of the virtual camera. These will significantly affect the quality of the datasets generated, and they may vary case by case.

3.5 Terrain Classifiers

We use deep learning methods to generate classifiers for our image segmentation dataset described in Section 3.4. Although this is a typical segmentation problem, and there are many deep learning frameworks we could use, we are targeting a specific inference platform: the Google Coral TPU [9], which imposes a particular

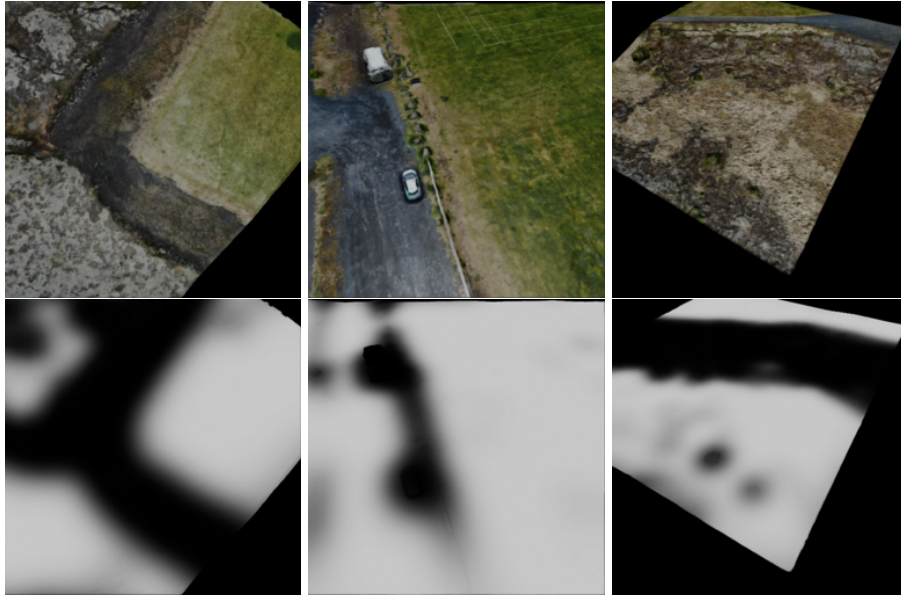


Fig. 4: Example images and masks from the synthetic data set.

toolchain revolving around Tensorflow [8,2], as well as a particular set of available operations, input sizes, etc.

We test the U-Net architecture for this task based on its well-known strong performance in segmentation problems. However, this is a non-exhaustive list, and other architectures could be applicable, e.g., auto-encoders, fully convolutional, and others. Additionally, initial experimentation revealed a few key notions. First, the little available memory on the Google Coral imposed size limitations of about 8 MB on our models and the input image resolution. Second, longer chains of operations, e.g., more sections in the U-Net architecture, significantly affected the framerate at which the Google Coral could perform inference, even when all of the overhead operations, such as playing/resizing video

Table 1: Datasets used to train the terrain classifiers. We use both LiDAR and photogrammetry (p-gram.) data.

Location	Type	Sensor	Data points	Source
1 RC airfield	p-gram. (oblique)	DJI H20T	750	own
2 RC airfield	LiDAR	DJI L2	750	own
3 Sheffield Cross	p-gram. (ortho)	unknown	241	WebODM
4 Soccer field	LiDAR	DJI L2	750	own
5 Soccer field	p-gram. (oblique)	DJI H20T	750	own
6 Summer house	p-gram. (oblique)	DJI H20T	750	own

and passing it to the TPU, were performed on a desktop machine and not on the more limited Raspberry Pi 5 to be used in the end product. Third, using RGB images as input to these small networks quickly resulted in them overfitting to both color and brightness. Therefore, we limited the image input size to 512x512 pixels, process grayscale images instead of RGB, and limited the number of U-Net sections to 3-4. We evaluate our models in terms of categorical accuracy and cross-entropy.

4 Results

4.1 Evaluation of Synthetic Segmentation Dataset

We have collected terrain data in Iceland at 3 locations via photogrammetry, and at 2 locations via LiDAR. We also use two open-source photogrammetry datasets available through WebODM. Table 1 lists the data sets used, and Figure 4 shows example pairs of images and masks from the soccer field dataset. Notably, the data sets from WebODM tend to contain only orthogonal photography, such that the models they produce appear realistic from a top-down view but less realistic from an angle, especially on vertical surfaces. We note additionally that the LiDAR reconstructions tend to capture smaller obstacles and deeper cracks much more accurately and make the surveys and subsequent data processing much quicker, on the scale of minutes to hours.

4.2 Synthetic Evaluation of Terrain Classifiers

We train a 4-stage U-Net with 512x512 resolution synthetic training and testing images for a maximum of 100 epochs with early stopping (monitoring the testing loss) with a patience of 15 epochs and with a learning rate of 5×10^{-5} with the Adam optimizer. We use categorical accuracy and categorical cross-entropy as our accuracy and loss metrics, respectively. The U-Net has four encoder steps, a bridge, and four decoder steps. The encoder block pipeline has a 2D convolution, batch normalization, leaky ReLU, 2D convolution, batch normalization, leaky ReLU, and maxpool. The decoder block pipeline has an upsampling layer, concatenation, 2D convolution, batch normalization, leaky ReLU, 2D convolution, batch normalization, and leaky ReLU. To conform with the available operations for the Google Coral, we remove batch normalization layers, replace upsampling with transpose convolution, and replace each leaky ReLU layer with a PReLU layer with an untrainable alpha parameter. We train in Keras [6] and quantize classifiers destined for the Google Coral to a TFLite model. This requires full quantization to unsigned 8-bit integers instead of the standard 32-bit float and also requires a representative dataset to tune the network during the conversion. The last step is to use the edge TPU compiler to convert the TFLite model into one compatible with the Google Coral. For each experiment, we select a subset of the datasets in Table 1 for training and testing. We run each experiment 10 times, taking the model with the lowest testing loss. This is feasible because the model is small, and the training time is 10-20 minutes. The result is presented in Table 2.

Table 2: Best classifier accuracy, loss, and real-world validation accuracy. The safety and danger thresholds for V2 are 0.6 and 0.4 respectively.

Classifier	Accuracy		Loss		Real-World	
	Training	Testing	Training	Testing	V1	V2
Best U-Net	0.667	0.815	0.613	0.373	0.778	0.833

4.3 Post-processing

Figure 5a shows an example prediction from the network at the 10-second mark (the last frame) of a video from the validation set. The network outputs two masks: one for safety and one for danger. For clarity, we only show the danger masks and other parts can be assumed safe. Setting thresholds for converting these to a binary mask is yet another parameter; we conduct a coarse parameter sweep, with the safety threshold θ_s being $[0.1, 0.2, 0.3, 0.4, 0.5, 0.6, 0.7, 0.8, 0.9]$ and the danger threshold being $1 - \theta_s$. The central square region represents a candidate landing site that we want to evaluate – in this case, an archery target (unsafe for landing) – and the evaluation is shown in the top left of the image. As explained in Section 3.2, this evaluation is determined by whether the majority of pixels in the square are considered safe or unsafe. The square is white if the area is considered safe and black if it is considered unsafe. Although many of the pixels in the box in Figure 5a are red, they are too sparse to reject the site – this can be seen in the safety prediction of 1.00, indicating that it has been deemed safe throughout the entire video. In the spirit of erring on the side of caution, we would like to reject unsafe landing sites despite the typical sparsity of unsafe classifications. We thus propose two post-processing enhancements: E1 is a box blur with the job of patching holes between rejected regions to create contiguous rejected regions, and E2 is temporal smoothing, with the job of keeping track of temporally sparse unsafe classifications. These are shown to reduce the safety prediction in Figure 5b and Figure 5c respectively. We experimented with values ranging from 1–10 frames for the temporal history and 7–19 for the box blur kernel size, ultimately choosing a box blur kernel size of 15 for E1 and a temporal history of 5 frames for E2. While E1 and E2 alone both reduce the safety prediction, only the combination of both completely reject the unsafe landing site with a prediction of 0.00, as shown in Figure 5d.

4.4 Real-World Evaluation of Terrain Classifiers

Using the landing site safety prediction method defined in Section 4.3, we conduct a secondary validation phase for the most promising classifiers. These results are presented in the last two columns of Table 2 – V1 represents the validation performance with safety and danger thresholds of 0.5, and V2 represents the validation performance with thresholds tuned through a coarse parameter search. We compare the network’s aggregated prediction to our knowledge of the area,

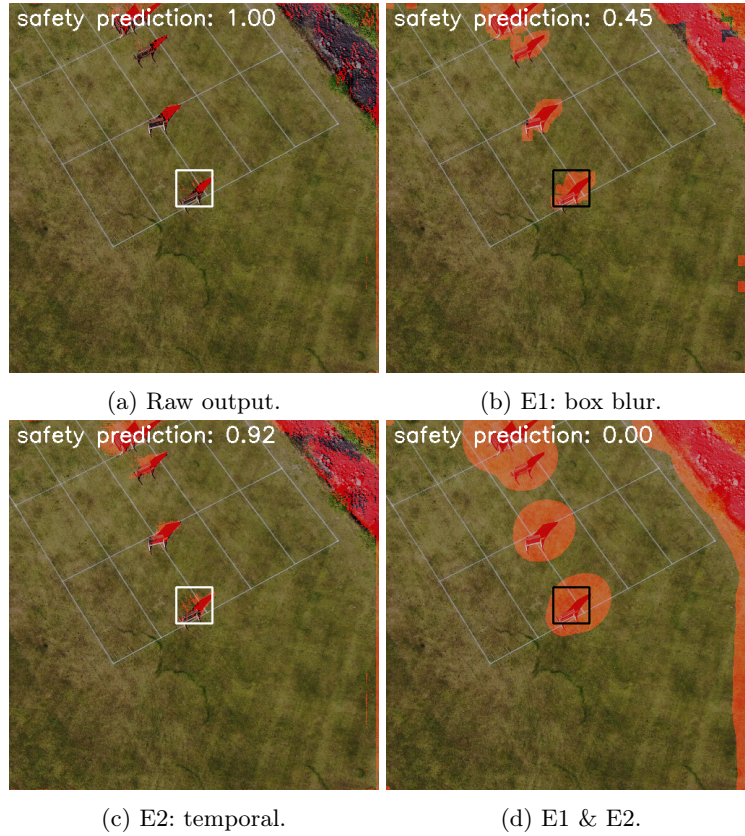


Fig. 5: Example predictions with and without post-processing

obtained by going to the area in person, and determine the network’s successful prediction rate over the validation locations in Figure 1. Overall, the best U-net correctly classifies 15 of 18 of the 10-second validation videos, i.e., it achieves an accuracy of 0.83, which we consider promising. The classifiers can run at a rate of about 3.4 Hz on the drone payload, which is fast enough for our task given that we can add filtering methods to make the approach smooth.

There were some important trends in the real-world evaluation. First, the classifiers almost universally classified a safe runway as unsafe and the unsafe, slanted gravel edge of a soccer field as safe. This seems to be a limitation of the fact that the classifier is appearance-based; the straight, monochromatic white runway markings seem to appear as tall structures, and the gravel does not change appearance significantly when slanted compared to when it is level (e.g., in a parking lot). Further, orientation and altitude are important factors, and performance is unsurprisingly much better if these are within the ranges of the synthetic training data, i.e., between 45 degrees below the horizon and vertically down, and at a distance of between 5 and 20 meters from the target. For exam-

ple, many classifiers correctly classified tall vegetation as unsafe when adequately close, and as safe when farther away. Finally, the small networks occasionally experience a “burn-in” where they produce persistently safe or unsafe classifications in particular locations of the image, regardless of the content of the image. This is most likely attributable to (1) disadvantageous initial conditions in the training process, and (2) biases in the data set, e.g., the fact that edges of the images are often unsafe as a result of being outside the generated terrain area, as shown in Figure 4.

In addition to lab tests, we conducted flights at multiple validation locations in the testing area, with the method running onboard the drone. The best way to showcase these experiments is with video: <https://vimeo.com/j0shua/mmm2025-demo>. The code for this project is available on Github [11].

5 Conclusion & Future Work

We presented a pipeline for generating terrain classifiers to find landing sites for a drone autonomously by analyzing video from the drone’s RGB camera. We automatically generated a synthetic dataset for image segmentation by reconstructing the terrain surveyed by the drone, labeling the reconstructed terrain geometrically for landing safety, and generating images and masks in simulation. We used both photogrammetry and LiDAR datasets and used one openly-available photogrammetry dataset from WebODM to show the method’s flexibility. We trained a U-Net on the synthetic dataset and quantified its performance in the real world by performing inference on 10-second drone videos of 18 known-safe and known-unsafe validation sites. The U-Nets correctly classified a maximum of 15 validation sites. Finally, we ran the method in real-time onboard a drone equipped with a Raspberry Pi 5 and Google Coral TPU, motivating our creation of a less than 1 MB network.

Future work should include collecting data from more real-world environments, and generating more synthetic data sets for training. More classifiers should be tested, e.g., auto-encoders, fully convolutional networks, and other segmentation methods such as support vector machines – with consideration of the constraints of embedded hardware so they can be embedded onboard a drone. It is also a point of interest to determine whether there is a difference in performance to be gained by either photogrammetry or LiDAR over the other. Finally, we will adapt this method so that it can generate commands to control the drone and execute the landings on its own, similar to the method in [22].

References

1. CloudCompare (version 2.12) [GPL software]. <http://www.cloudcompare.org/> (2023), Retrieved from <https://github.com/CloudCompare/CloudCompare>
2. Authors, T.: TensorFlow Lite: Lightweight solution for mobile and embedded devices. <https://www.tensorflow.org/lite> (2017), <https://www.tensorflow.org/lite>, version 2.11.0

3. Barnes, D., Maddern, W., Posner, I.: Find your own way: Weakly-supervised segmentation of path proposals for urban autonomy. In: 2017 IEEE International Conference on Robotics and Automation (ICRA). pp. 203–210 (2017). <https://doi.org/10.1109/ICRA.2017.7989025>
4. Beycimen, S., Ignatyev, D., Zolotas, A.: A comprehensive survey of unmanned ground vehicle terrain traversability for unstructured environments and sensor technology insights. *Engineering Science and Technology, an International Journal* **47**, 101457 (2023). <https://doi.org/https://doi.org/10.1016/j.jestch.2023.101457>
5. Chen, L., Xiao, Y., Yuan, X., Zhang, Y., Zhu, J.: Robust autonomous landing of UAVs in non-cooperative environments based on comprehensive terrain understanding. *Science China Information Sciences* **65**(11), 212202 (2022). <https://doi.org/10.1007/s11432-021-3429-1>
6. Chollet, F., et al.: Keras. <https://keras.io> (2015)
7. Corporation, N.: Isaac Sim (2024), <https://developer.nvidia.com/isaac-sim>
8. Developers, T.: Tensorflow (Jul 2024). <https://doi.org/10.5281/zenodo.12726004>
9. Google: Coral Edge TPU. <https://coral.ai/> (2023), accessed: 2023-08-02
10. Hackel, T., Wegner, J.D., Schindler, K.: Contour Detection in Unstructured 3D Point Clouds. In: 2016 IEEE Conference on Computer Vision and Pattern Recognition (CVPR). pp. 1610–1618 (2016). <https://doi.org/10.1109/CVPR.2016.178>
11. Joshua Springer: Unstructured Landing Site Identification Repository. https://github.com/uzgit/unstructured_landing_site_identification_mmm2025 (2024), accessed: 2024-10-17
12. Kakaletsis, E., Symeonidis, C., Tzelepi, M., Mademlis, I., Tefas, A., Nikolaidis, N., Pitas, I.: Computer Vision for Autonomous UAV Flight Safety: An Overview and a Vision-based Safe Landing Pipeline Example. *ACM Comput. Surv.* **54**(9) (oct 2021). <https://doi.org/10.1145/3472288>
13. Kazhdan, M., Bolitho, M., Hoppe, H.: Poisson surface reconstruction. In: Proceedings of the Fourth Eurographics Symposium on Geometry Processing. p. 61–70. SGP '06, Eurographics Association, Goslar, DEU (2006)
14. Loftmyndir ehf.: <https://map.is/> (2024), accessed: 2024-10-17
15. Marcu, A., Costea, D., LicăreȚ, V., Pîrvu, M., Slușanschi, E., Leordeanu, M.: SafeUAV: Learning to Estimate Depth and Safe Landing Areas for UAVs from Synthetic Data. In: Leal-Taixé, L., Roth, S. (eds.) *Computer Vision – ECCV 2018 Workshops*. pp. 43–58. Springer International Publishing, Cham (2019)
16. Marcu, A., Licaret, V., Costea, D., Leordeanu, M.: Semantics Through Time: Semi-supervised Segmentation of Aerial Videos with Iterative Label Propagation, pp. 537–552 (02 2021). https://doi.org/10.1007/978-3-030-69525-5_32
17. Maturana, D., Scherer, S.: 3D Convolutional Neural Networks for landing zone detection from LiDAR. *Proceedings - IEEE International Conference on Robotics and Automation* **2015**, 3471–3478 (06 2015). <https://doi.org/10.1109/ICRA.2015.7139679>
18. Mitroudas, T., Tsintotas, K.A., Santavas, N., Psomoulis, A., Gasteratos, A.: Towards 3D printed modular unmanned aerial vehicle development: The landing safety paradigm. In: 2022 IEEE International Conference on Imaging Systems and Techniques (IST). pp. 1–6 (2022). <https://doi.org/10.1109/IST55454.2022.9827665>
19. Pluckter, K., Scherer, S.: Precision UAV Landing in Unstructured Environments. In: Xiao, J., Kröger, T., Khatib, O. (eds.) *Proceedings of the 2018 International Symposium on Experimental Robotics*. Springer Proceedings in Advanced

- Robotics, vol. 11, pp. 177—187. Springer, Cham (2018). https://doi.org/10.1007/978-3-030-33950-0_16
20. Ronneberger, O., Fischer, P., Brox, T.: U-Net: Convolutional Networks for Biomedical Image Segmentation. In: Navab, N., Hornegger, J., Wells, W.M., Frangi, A.F. (eds.) *Medical Image Computing and Computer-Assisted Intervention – MICCAI 2015*. pp. 234–241. Springer International Publishing, Cham (2015). https://doi.org/10.1007/978-3-319-24574-4_28
 21. Springer, J., Þór Guðmundsson, G., Kyas, M.: A Precision Drone Landing System using Visual and IR Fiducial Markers and a Multi-Payload Camera (2024), <https://arxiv.org/abs/2403.03806>
 22. Springer, J., Þór Guðmundsson, G., Kyas, M.: A Precision Drone Landing System using Visual and IR Fiducial Markers and a Multi-Payload Camera (2024), <https://arxiv.org/abs/2403.03806>
 23. Springer, J., Þór Guðmundsson, G., Kyas, M.: Lowering Barriers to Entry for Fully-Integrated Custom Payloads on a DJI Matrice (2024), <https://arxiv.org/abs/2405.06176>
 24. Symeonidis, C., Kakaletsis, E., Mademlis, I., Nikolaidis, N., Tefas, A., Pitas, I.: Vision-based UAV Safe Landing exploiting Lightweight Deep Neural Networks. In: *Proceedings of the 2021 4th International Conference on Image and Graphics Processing*. p. 13–19. ICIGP '21, Association for Computing Machinery, New York, NY, USA (2021). <https://doi.org/10.1145/3447587.3447590>
 25. Sánchez, M., Martínez, J.L., Morales, J., Robles, A., Morán, M.: Automatic Generation of Labeled 3D Point Clouds of Natural Environments with Gazebo. In: *2019 IEEE International Conference on Mechatronics (ICM)*. vol. 1, pp. 161–166 (2019). <https://doi.org/10.1109/ICMECH.2019.8722866>
 26. Tang, L., Ding, X., Yin, H., Wang, Y., Xiong, R.: From one to many: Unsupervised traversable area segmentation in off-road environment. In: *2017 IEEE International Conference on Robotics and Biomimetics (ROBIO)*. pp. 787–792. <https://doi.org/10.1109/ROBIO.2017.8324513>
 27. Toffanin, P., Leo, L.D., Chamo, N., Farell, K., Saijin-Naib, Mather, S., Barker, B., Davis, B., Kaluza, O., pyup.io bot, Joseph, D., IZem, A., Bateman, C., Islam, T., USPLM, POULAIN, S., Acuña, D., Mahesh, A., Machado, R.W., Ves, N., Mumby, P., Pereira, P.J., İbrahim Sarıççek, vinsonliux, w toguchi83, mateo3d, Fitzsimmons, S., Bazile, R., Heggy, I.: *OpenDroneMap/WebODM: 2.5.4* (Jul 2024). <https://doi.org/10.5281/zenodo.12775235>